

Hopf Bifurcation of the Unsteady Regularized Driven Cavity Flow

JIE SHEN

*Department of Mathematics and The Institute for Applied Mathematics
and Scientific Computing, Indiana University, Bloomington, Indiana 47405*

Received April 25, 1989; revised May 22, 1990

A numerical simulation of the unsteady incompressible flow in the unit cavity is performed by using a Chebyshev–Tau approximation for the space variables. The high accuracy of the spectral methods and the condensed distribution of the Chebyshev-collocation points near the boundary enable us to obtain reliable results for high Reynolds numbers with a moderate number of modes. It is found that the flow converges to a stationary state for Reynolds numbers (Re) up to 10,000; for Reynolds numbers larger than a critical value $10,000 < Re_1 \leq 10,500$ and less than another critical value $15,000 < Re_2 \leq 15,500$, the flow becomes periodic in time which indicates a Hopf bifurcation; the flow loses time periodicity for $Re \geq Re_2$. © 1991 Academic Press, Inc.

1. INTRODUCTION

With the rapid increase in computing power, we can now envisage solving dynamical systems for ranges of values of physical parameters leading to nontrivial dynamical features such as Hopf bifurcations, transitions to turbulence, etc. (see, for instance, [6, 3]). On the other hand, newly developed theoretical models, such as attractors, determining modes, inertial manifolds, etc. (see [14] for a review of these aspects), lead to a better understanding of complex physical phenomena.

Gustafson and Halasi [6] found a persistent oscillation in the rectangular driven cavity flow of aspect ratio equal to 2 at $Re = 10,000$ by integrating the unsteady Navier–Stokes equations (NSE). This led us to conjecture that as the Reynolds number increases to a certain critical value, the same kind of dynamical behavior as in the rectangular cavity flow might be observed in the unit cavity flow. The aim of this paper is to confirm this conjecture and try to locate the critical Reynolds numbers within a relatively small range. Let us also mention that very recently Bruneau and Jouron [1] observed transitions to turbulence in the unit cavity flow for a Reynolds number lower than 7500 by solving the steady NSE with a high resolution grid.

Due to the presence of a thin boundary layer (of the order $O(Re^{-1/2})$), a very fine grid near the boundary should be used for high Reynolds numbers to ensure a proper resolution to the boundary layer. Consequently an irregular grid condensing near the boundary is desirable to minimize the number of unknowns.

However, most of the authors used a uniform grid for which efficient algorithms are available, despite the fact that a huge number of unknowns was involved for high Reynolds numbers.

It is well known that the zeros of Chebyshev polynomials are condensed near the boundary. In fact the distance between the adjacent zeros of the N th Chebyshev polynomial near the boundary is of the order $O(N^{-2})$. In addition, the spectral methods using Chebyshev polynomials achieve spectral accuracy for smooth functions. These nice properties lead us to choose the Chebyshev–Tau formulation (see, for instance, [12 or 2]) for the space variables. In order to take advantage of the spectral accuracy, we consider a regularized driven cavity flow where the singularity at the upper corners is removed. Namely, we take the horizontal speed on the upper lid of the cavity to be $16x^2(1-x)^2$ instead of 1. Since the velocity distribution along the upper wall now is weaker than that of the driven cavity flow, it is clear that the effective Reynolds numbers would be different for the two flows, as are some quantitative characteristics of the flow such as the magnitude and the location of the center of the vortices. Although this regularization is less physical, it is expected that the regularized driven cavity flow preserves qualitatively the dynamical properties of the driven cavity flow. However, as mentioned above, since the effective Reynolds number of the flow with unsmoothed boundary conditions is larger than that of the flow with regularized boundary conditions, we would expect that if the regularized driven cavity flow exhibits Hopf bifurcations at certain critical Reynolds number, then the driven cavity flow will also exhibit Hopf bifurcations at a smaller critical Reynolds number.

In [13], we started to investigate the dynamical behaviors of the regularized driven cavity flow. We presented there some preliminary results which indicated that Hopf bifurcations occurred at $Re = 12,000$. Due to a limitation of the computing source, the approximating solutions presented there had not been developed in final asymptotic states. In this paper, we continue the investigation initiated in [13], and intend to give more detailed and accurate characterizations for the nonstationary solutions of the regularized driven cavity flow.

By integrating the unsteady NSE with the regularized boundary conditions, we found stationary solutions for Reynolds numbers up to 10,000. For $Re = 10,500$, no steady solution was found; instead, after a long transient time, the flow finally became periodic in time which indicated that a Hopf bifurcation occurs at a critical Reynolds number in $(10,000, 10,500]$. As we further increase the Reynolds number, the qualitative behavior, namely the time periodicity, of the flow remained the same for Reynolds numbers up to 15,000. For $Re = 15,500$, the flow lost its time periodicity and became quasi-periodic. This indicates that another bifurcation occurs at a critical Reynolds number in $(15,000, 15,500]$. One would expect that further increase of the Reynolds number would lead to a totally turbulent flow.

The paper is organized as follows. In Section 2, we present the numerical algorithms for the computation, namely the spatial and temporal discretizations of the NSE. Then in Section 3, we present various results on the regularized driven cavity flow for a wide range of the Reynolds number.

2. NUMERICAL SCHEMES

The 2D unsteady incompressible NSE in the primitive variable formulation are written as:

$$\begin{aligned} \frac{\partial u}{\partial t} - \nu \Delta u + (u \cdot \nabla) u + \nabla p &= f, & (x, y) \text{ in } \Omega, \\ \operatorname{div} u &= 0, & (x, y) \text{ in } \Omega. \end{aligned} \quad (1)$$

with appropriate boundary conditions. The unknowns are the vector function u (velocity) and the scalar function p (pressure). In this paper, we will restrict ourselves to the unit cavity, i.e., $\Omega = [0, 1] \times [0, 1]$.

2.1. Spatial Discretization

As we will see later, after temporal discretizations of (1) by semi-implicit schemes (i.e., the viscous term is treated implicitly while leaving the non-linear term explicit), at each time step we will only need to solve a series of Helmholtz equations with Dirichlet or Neumann boundary conditions. Consequently, an efficient algorithm for solving the Helmholtz equation is desirable. We have chosen the Chebyshev–Tau approximation for the Helmholtz equation since the diagonalization procedure (see [7]) associated with this formulation is a very robust Helmholtz solver.

Let us denote P_N to be the space of polynomials of order less or equal than N ; $\mathcal{P}_N = P_N \times P_N$. Then the Chebyshev–Tau approximation of the 2D Helmholtz equation reads

$$(\alpha u - \Delta u, v)_\omega = (f, v)_\omega, \quad \forall v \in \mathcal{P}_{N-2}, \quad (2)$$

where $u \in \mathcal{P}_N$ satisfying some appropriate boundary conditions and ω is the weight function associated with the base functions of P_N , namely, $\omega = 1$ for the Legendre polynomials and $\omega = (1 - x^2)^{-1/2} \cdot (1 - y^2)^{-1/2}$ for the Chebyshev polynomials. It is proven (see, for example, [12]) that the system (3) admits a unique solution. In addition, this solution converges to the solution of the Helmholtz equation exponentially, provided smoothness of the solution. We refer to [12] for a detailed investigation of this formulation.

2.2. Temporal Discretizations

The velocity and the pressure are coupled together by the incompressibility condition which makes the equations difficult to solve. The classical projection scheme (or fractional step scheme, see, for instance, [15]) decouples the velocity and the pressure, but it suffers from large splitting errors at the boundary. Kim and Moin [8] proposed a second-order projection scheme which removes the large splitting errors at the boundary while keeping the simplicity of the projection

scheme. We will use their scheme for the temporal discretization in conjunction with a Chebyshev–Tau space discretization. The scheme reads as follows without discretizing the space variables:

$$\begin{aligned} & \frac{1}{\Delta t} (u^* - u^n) - \frac{\nu}{2} \Delta (u^* + u^n) \\ &= \frac{3}{2} (f(n \cdot \Delta t) - (u^n \cdot \nabla) u^n) - \frac{1}{2} (f((n-1) \cdot \Delta t) - (u^{n-1} \cdot \nabla) u^{n-1}), \end{aligned} \quad (3)$$

$$u^*|_{\partial\Omega} = u((n+1) \Delta t) + \Delta t \nabla \phi^n,$$

and

$$\begin{aligned} & \frac{1}{\Delta t} (u^{n+1} - u^*) + \nabla \phi^{n+1} = 0, \\ & \operatorname{div} u^{n+1} = 0, \\ & u^{n+1} \cdot \mathbf{n}|_{\partial\Omega} = u((n+1) \Delta t) \cdot \mathbf{n}. \end{aligned} \quad (4)$$

In the first step, we solve an intermediate velocity u^* which is not physical. In fact, u^* does not satisfy the incompressibility condition. Then, in the second step we project u^* onto the divergence free space to get an adequate velocity approximation u^{n+1} . We note that ϕ^{n+1} in the scheme is not a proper approximation of the original pressure, since we can derive from (3)–(4) that

$$\frac{\partial \phi^{n+1}}{\partial \mathbf{n}} = \frac{\partial \phi^n}{\partial \mathbf{n}} = \dots = \frac{\partial \phi^1}{\partial \mathbf{n}}, \quad \forall n,$$

which is certainly not satisfied by the exact pressure. We will show below that a proper approximation for the pressure is given by

$$p^{n+1} = \phi^{n+1} - \frac{\Delta t \nu}{2} \Delta \phi^{n+1}. \quad (5)$$

We derive from (4) that

$$u^* = u^{n+1} + \Delta t \nabla_{\phi}^{n+1}.$$

Now we replace u^* in (3) by the above formula, taking into account (5), we obtain

$$\begin{aligned} & \frac{1}{\Delta t} (u^{n+1} - u^n) - \frac{\nu}{2} \Delta (u^{n+1} + u^n) + \nabla p^{n+1} \\ &= \frac{3}{2} (f(n \cdot \Delta t) - (u^n \cdot \nabla) u^n) - \frac{1}{2} (f((n-1) \cdot \Delta t) - (u^{n-1} \cdot \nabla) u^{n-1}), \end{aligned} \quad (6)$$

$$\operatorname{div} u^{n+1} = 0,$$

with the boundary conditions

$$\begin{aligned} u^{n+1} \cdot \mathbf{n}|_{\partial\Omega} &= u((n+1)\Delta t) \cdot \mathbf{n}, \\ u^{n+1} \cdot \boldsymbol{\tau}|_{\partial\Omega} &= u((n+1)\Delta t) \cdot \boldsymbol{\tau} - \Delta t \nabla(\phi^{n+1} - \phi^n) \cdot \boldsymbol{\tau}. \end{aligned} \tag{7}$$

The scheme (6) with these boundary conditions is nothing else than the second-order Crank–Nicolson–Adams–Bashforth scheme with an $O(\Delta t^2)$ deviation in the tangent direction of the boundary. It follows that u^{n+1} , is a second-order approximation of $u((n+1)\Delta t)$. (See [14] for more precise error estimates on the projection methods.)

By applying the divergence operator to (4), we find that (4) is equivalent to (taking $\phi^1 = 0$)

$$\begin{aligned} \Delta\phi^{n+1} &= \frac{1}{\Delta t} \operatorname{div} u^*, \\ \frac{\partial\phi^{n+1}}{\partial\mathbf{n}} \Big|_{\partial\Omega} &= 0, \\ u^{n+1} &= u^* - \Delta t \nabla\phi^{n+1}. \end{aligned} \tag{8}$$

Therefore, at each time step, we only need to solve one vector Helmholtz equation (3) and one scalar Helmholtz equation (8).

Since no results for $\operatorname{Re} \geq 1000$ were available for the regularized driven cavity flow given the author’s knowledge, in order to double-check our results, we have implemented also the following first-order semi-implicit scheme:

$$\begin{aligned} \frac{1}{\Delta t} (u^{n+1} - u^n) - \nu \Delta u^{n+1} + \nabla p^{n+1} &= f(n\Delta t) - (u^n \cdot \nabla) u^n, \\ \operatorname{div} u &= 0, \\ u^{n+1}|_{\partial\Omega} &= u((n+1)\Delta t). \end{aligned} \tag{9}$$

Knowing u^n , the system (9) is nothing more than a generalized Stokes equation. We approximate it by the influenced matrix method (see, for instance, [9, 11]) which transforms the generalized Stokes equation into two vector Helmholtz equations and two scalar Poisson equations with the aid of a pre-computed influenced matrix. This matrix, of the order of $(4N - 5) \times (4N - 5)$ if $(N + 1) \times (N + 1)$ modes used for the spatial discretization, can be used repeatedly at each time step for a fixed combination of $(N, \nu, \Delta t)$. However, the computation of this matrix involves the inversion of a full matrix of the same order; double precision is then advisable for the computation of this influenced matrix for relatively large N .

From now on, we will refer to the first-order scheme (9) with the influenced matrix technique as the first scheme, and the second-order projection scheme (3)–(4) with the Chebyshev–Tau space discretization as the second scheme. We should point out that the time discretization error of (9) does not affect the preci-

sion of approximate stationary solutions. However, due to the splitting error introduced by the projection method, the approximate stationary solutions obtained by using the second scheme do depend on the time discretization error, so that a sufficiently small time step should be used to achieve the desired accuracy. On the other hand, the precision of approximate nonstationary solutions depends on the time discretization errors. Since the first scheme is only of first order, all the nonstationary solutions presented below are obtained by using the second scheme.

3. NUMERICAL RESULTS AND DISCUSSIONS

The numerical computations were made on an Alliant FX/8 with four processors. Double precision was used for all the computations to increase the reliability of the results. The non-linear term was computed by the transform method (or pseudo-spectral method, see [10]). The transformation between the physical space and the spectral space was made directly by the standard matrix multiplication subroutine in the Alliant scientific library. Direct multiplication turned out to be more efficient for moderate N (up to $N \times N = 65 \times 65$) than using the FFT on this parallel computer especially when $N - 1$ was not a power of 2.

In Table I, we list the cpu per time step for both schemes. We observe that the first scheme is roughly 35% more time consuming than the second one for each time step.

As explained in the Introduction, in order to take advantage of the high accuracy of the spectral space discretization, we consider the so-called regularized driven cavity flow. The boundary conditions for the regularized driven cavity flow are $u = (16x^2(1-x)^2, 0)$ on the upper lid and $u = (0, 0)$ on other parts of the boundary. The initial condition was taken to be 0 for all the computations unless otherwise specified.

3.1. Stationary Solutions

To test our schemes, we have run both schemes with Reynolds numbers up to 10,000, and we have always obtained stationary solutions. We should point out that

TABLE I
Cpu per Time Step

Number of modes	Cpu in seconds for first scheme	Cpu in seconds for second scheme
17×17	0.089	0.063
25×25	0.164	0.122
33×33	0.269	0.218
49×49	0.647	0.472
65×65	1.202	0.928

TABLE II
Time Step and Convergence Speed

Re	No. of modes	1st	Scheme	2nd	Scheme
		Δt	No. of iter.	Δt	No. of iter.
100	17 × 17	4.0	38	0.4	260
400	17 × 17	0.5	390	0.3	600
1000	25 × 25	0.15	1750	0.15	1780
2000	25 × 25	0.1	4420	0.12	3910
5000	33 × 33	0.03	28800	0.05	18100

even though we have found a stationary solution for $Re = 10,000$, our results are not in contradiction with those presented in [1] because the effective Reynolds numbers for the driven cavity flow and for the regularized driven cavity flow are different. As mentioned in the Introduction, it is expected that the driven cavity flow would lose its stability at a Reynolds number less than 10,000.

The differences between the two approximate solutions provided by the two schemes are of order $O((\Delta t)^2)$ due to the splitting errors committed by the projection method. This also confirms that the projection scheme we used is indeed second order. Both schemes are only conditionally stable due to the explicit treat-

TABLE III
Some Characteristics of the Stream Functions

Re	Primary vortex	Secondary vortex bottom right	Secondary vortex bottom left	Secondary vortex upper left
100 (17 × 17)	-0.08368 (0.609, 0.750)	4.6676E-6 (0.953, 0.047)	1.3987E-6 (0.031, 0.031)	—
400 (17 × 17)	-0.08584 (0.578, 0.625)	1.9774E-4 (0.922, 0.094)	6.3146E-6 (0.031, 0.047)	—
1000 (25 × 25)	-0.08719 (0.547, 0.578)	5.6762E-4 (0.922, 0.094)	8.2841E-5 (0.078, 0.063)	—
2000 (25 × 25)	-0.08762 (0.531, 0.547)	8.0667E-4 (0.922, 0.094)	3.1772E-4 (0.078, 0.094)	1.4497E-5 (0.031, 0.092)
2000 (33 × 33)	-0.08776 (0.531, 0.547)	8.0841E-4 (0.922, 0.094)	3.5432E-4 (0.094, 0.094)	1.7143E-5 (0.031, 0.092)
5000 (33 × 33)	-0.08803 (0.516, 0.531)	7.7475E-4 (0.922, 0.94)	7.5268E-4 (0.094, 0.094)	6.7780E-4 (0.078, 0.092)
10000 (49 × 49)	-0.08824 (0.536, 0.531)	3.2494E-4 (0.922, 0.094)	7.9246E-4 (0.094, 0.094)	1.4860E-3 (0.094, 0.092)

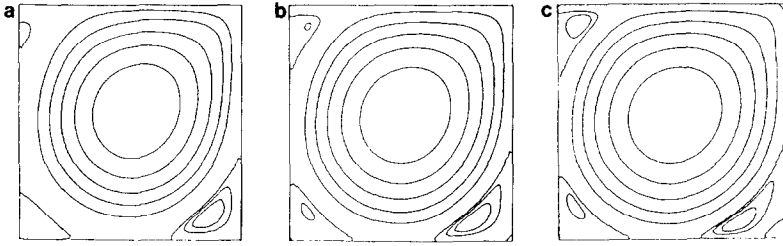


FIG. 1. Streamlines: (a) $Re = 2000$; (b) $Re = 5000$; (c) $Re = 10,000$.

ment of the non-linear term. Unfortunately, the critical time step Δt_c (i.e., the scheme is stable when $\Delta t \leq \Delta t_c$) varies with Re and the number of modes N non-linearly, and it can only be determined by numerical experiments. In Table II the time steps Δt and the number of steps used to get maximal residual less than $1.0E-6$ are given. Our experiments show that the time steps in the Table II are very close to Δt_c . This indicates that Δt_c is not very restrictive with respect to Re and N . We also observe that as Re and N increase, Δt_c of the second scheme becomes less restrictive than that of the first scheme.

In Table III the magnitudes and the locations of the centres (based on the 65×65 uniform grid) of the primary and secondary vortices for some Reynolds numbers are given. In order to eliminate the time discretization error, all the results reported in Table III are obtained by using the first scheme. Note that two results at $Re = 2000$ with different space discretization modes are given for comparison. We also plot the streamline contours at $Re = 2000$ from these two results together on the same paper (see Fig. 1a). We note that the difference between them is too small to be visible in the figure. This indicates that the flow at $Re = 2000$ can be very well represented with only 25×25 modes, thanks to the condensed distribution of the Chebyshev-collocation points near the boundary.

The streamline contours and the normalized velocity fields for $Re = 5000$ and $Re = 10,000$ are also presented in the Figs. 1 and 2. At $Re = 2000$, a secondary vortex appears at the top left of the cavity; a tertiary vortex becomes visible at the bottom right of the cavity at about $Re = 5000$; another tertiary vortex appears at

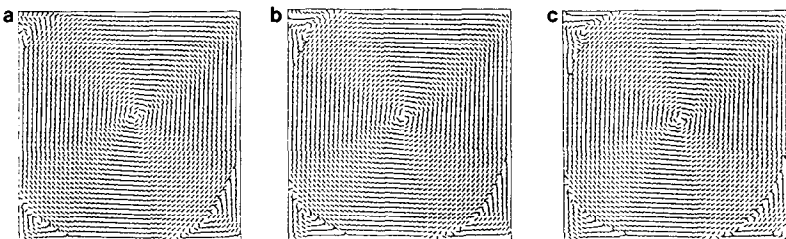


FIG. 2. Velocity field: (a) $Re = 2000$; (b) $Re = 5000$; (c) $Re = 10,000$.

the top right corner at $Re = 10,000$. We observe that the vortex dynamics of the regularized driven cavity flow is similar to that of the driven cavity flow although the quantitative characteristics for the two flows are somewhat different (see, for instance, [4] and the references therein for a detailed presentation of the driven cavity flow).

3.2. Nonstationary solutions

Since the second-order projection scheme is more economical and accurate for time-dependent problems, all the results reported below are obtained by using the second scheme with time step fixed at $\Delta t = 0.02$.

Taking the steady solution at $Re = 10,000$ as the initial data, we started to run the second scheme with $Re = 10,500$ by using 49×49 modes. The approximate solution quickly developed into a time periodic pattern, although it actually took a very long time for the solution to attain its final asymptotic periodic state. The main measure we used to determine whether a flow had attained its final asymptotic state was the total kinetic energy:

$$E(n \Delta t) = \left\{ \sum_{i,j=0}^{N-1} [(u_{i,j}^n)^2 + (v_{i,j}^n)^2] \right\}^{1/2},$$

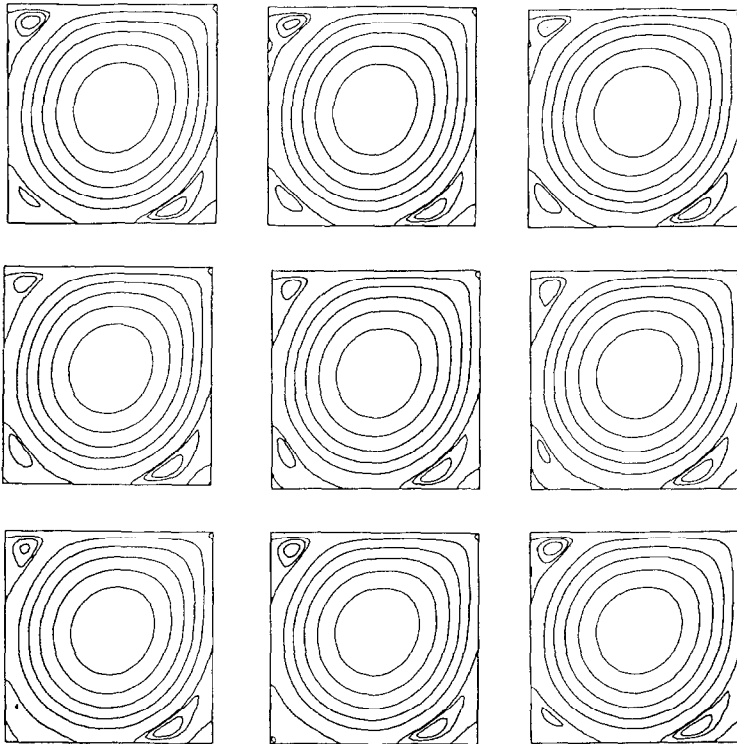


FIG. 3. One complete cycle of streamline contours at time interval of 1.52.

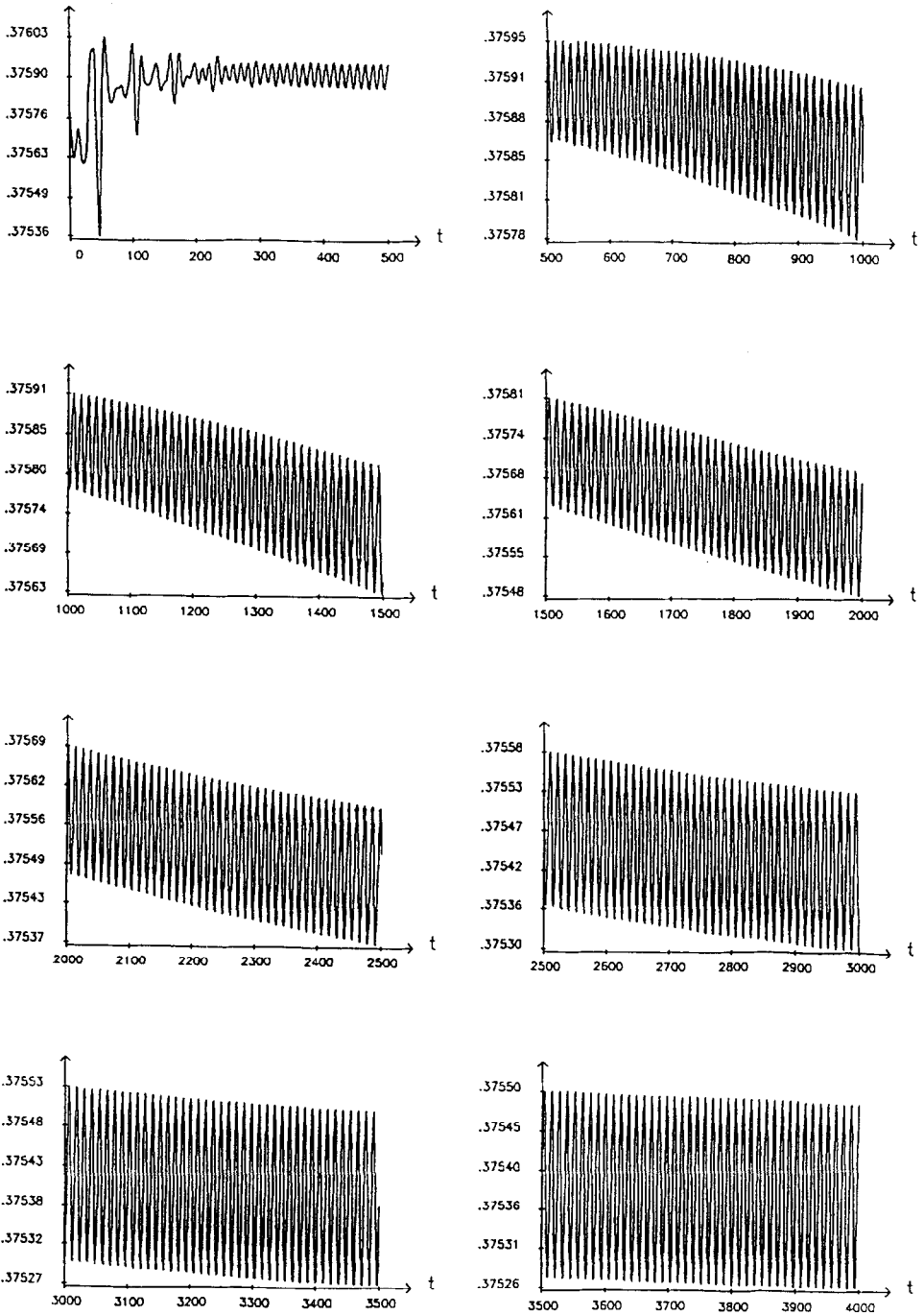


FIG. 4. Convergence histories of kinetic energy of the flow at $Re = 10,500$ with 49×49 modes.

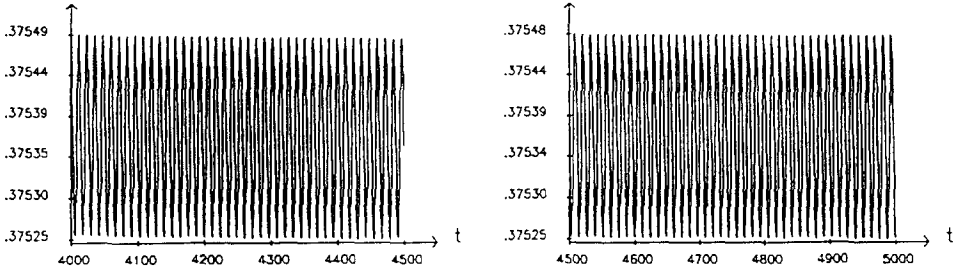


FIGURE 4—Continued

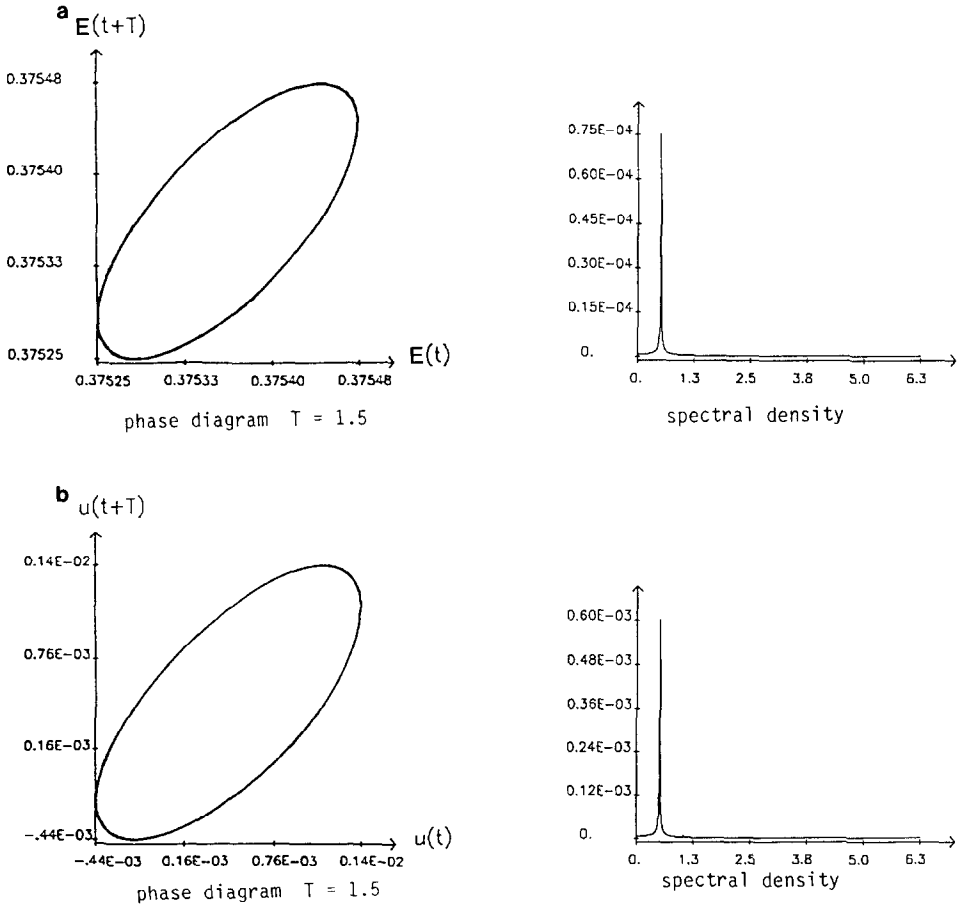


FIG. 5. (a) Kinetic energy at $Re = 10,500$ with 49×49 modes. (b) The first component of velocity at $(x, y) = (0.038, 0.990)$, $Re = 10,500$ with 49×49 modes.

where $u_{i,j}^n, v_{i,j}^n$ are the (i, j) th coefficients of the Chebychev expansion of the two components of the velocity at the n th step. The convergence histories of the kinetic energy of the solution are presented in the Fig. 4. We see clearly from Fig. 4 that the solution reaches its asymptotic periodic state at about $t = 4500$. In Fig. 5, we present the phase diagrams and the spectral density of the kinetic energy and the first component of velocity at a particular point $(x, y) = (0.038, 0.990)$, based on the data taken at 50,000 time steps which are about 82.5 complete cycles, after the flow reached its asymptotic periodic state. Those plots indicate a perfect periodic pattern for our asymptotic solutions. To exhibit the global asymptotic state of the flow, in Fig. 3 we plot a series of nine streamline contours at time interval of 1.52 such that the nine plots make one complete cycle. We observe that there are persistent oscillations at all the secondary and tertiary vortices. The most significant changes during one period are the periodic appearance and disappearance of two tertiary vortices

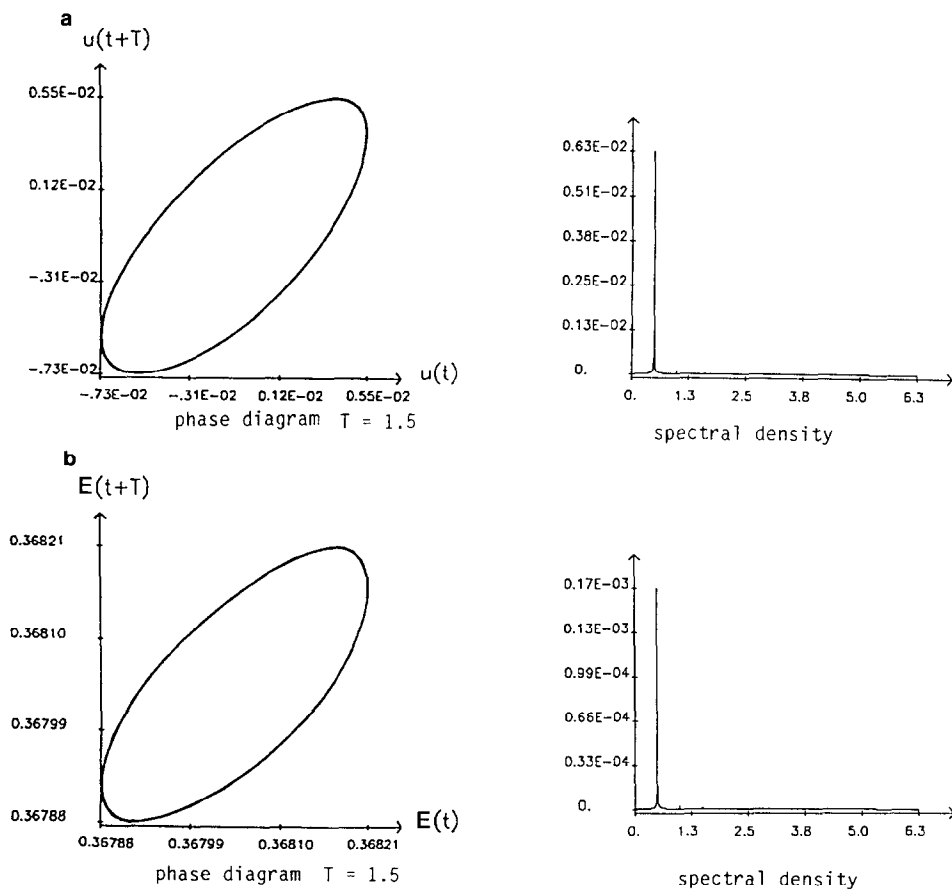


FIG. 6. (a) The first component of velocity at $(x, y) = (0.084, 0.990)$, $Re = 14,000$ with 65×65 modes. (b) The kinetic energy at $Re = 14,000$ with 65×65 modes.

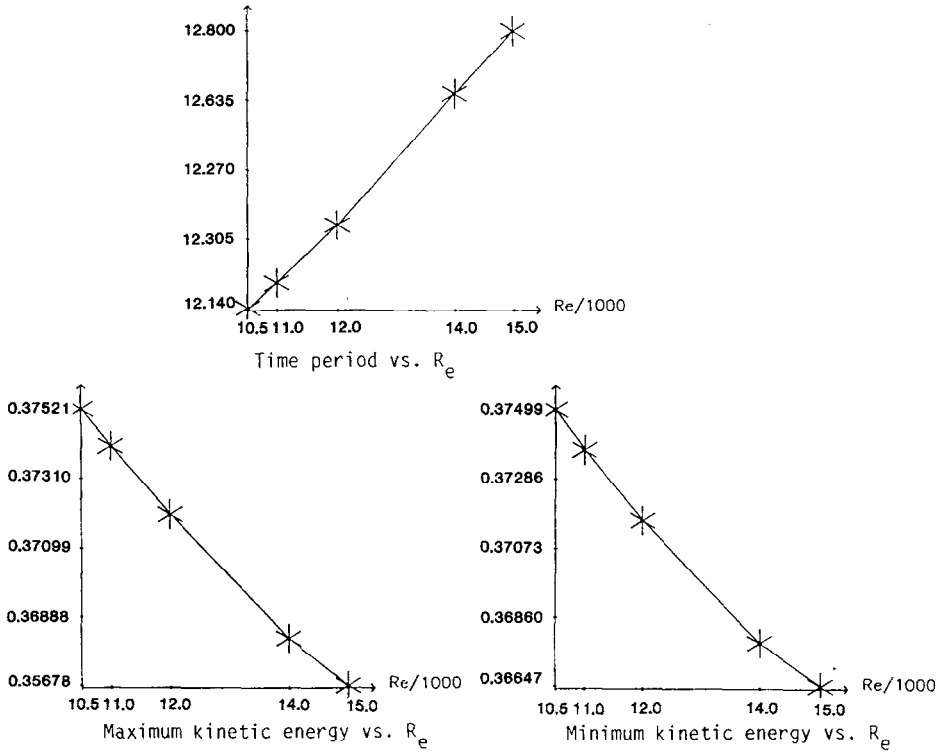


FIG. 7. The dependency of the time periodic solutions on Re .

TABLE IV
The Dependency of the Periodic Solutions on Re

Re	Time period	Maximum kinetic energy	Minimum kinetic energy
10500 (48 × 48)	12.12	0.37548	0.37525
10500 (64 × 64)	12.14	0.37521	0.37499
11000 (48 × 48)	12.22	0.37438	0.37402
11000 (64 × 64)	12.20	0.37411	0.37375
12000 (64 × 64)	12.34	0.37202	0.37160
14000 (64 × 64)	12.65	0.36822	0.36780
15000 (64 × 64)	12.80	0.36678	0.36647

at the bottom left and at the top left. We observe that the streamline contour pattern at the beginning of the cycle is perfectly recaptured at the end of the cycle. This strongly indicates the global periodic feature of the solution in the entire domain.

To ensure that the computed periodic solution was not a numerical artifact, we have also run the scheme for $Re = 10,500$ with 65×65 modes. Although it took a longer time to attain the final asymptotic state (at about $t = 7000$), we found that the period and the maximum and the minimum of the kinetic energy of the solutions obtained by using those two different grids were essentially the same (see Table IV) and the two asymptotic states were both qualitatively and quantitatively consistent. We can then conclude that the regularized driven cavity flow possesses a Hopf bifurcation at a critical number $Re \in (10,000, 10,500]$.

Let us mention that most recently in [5] which was a continued study of [6], Goodrich, Gustafson, and Halasi have given a very detailed investigation for the rectangular driven cavity flow at $Re = 5000$. The qualitative behaviors of their asymptotic solution were very similar to those presented here.

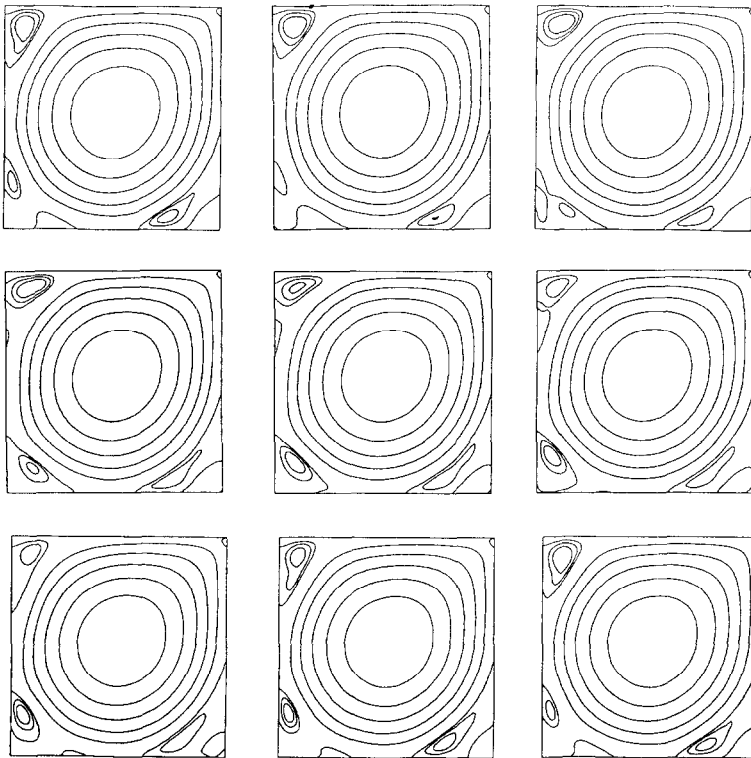


FIG. 8. One complete cycle of streamline contours at $Re = 14,000$ with 65×65 modes at time interval of 1.59.

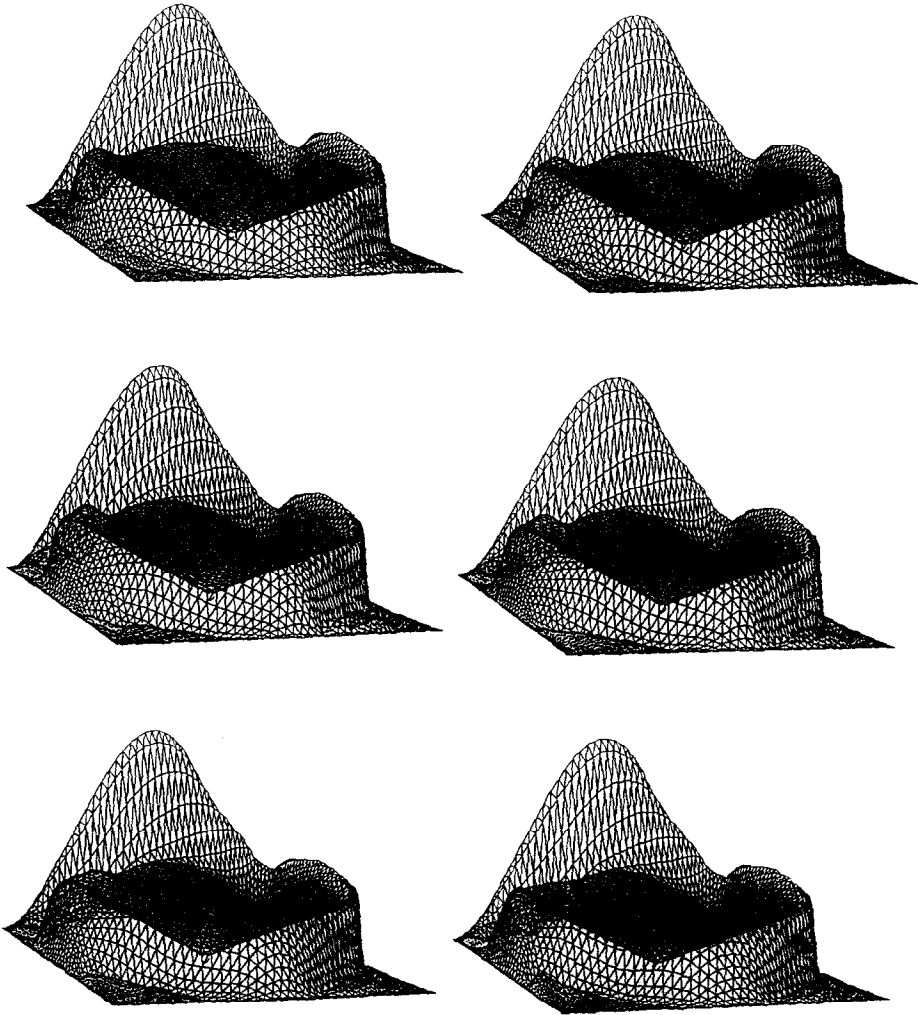


FIG. 9. One complete cycle of the surface of the kinetic energy at $Re = 14,000$ with 65×65 modes at time interval of 1.59.

One would expect for Re larger than another critical number Re_2 , the solution would lose time periodicity and its temporal variation would become more complex. Still using 65×65 modes, we went on to increase the Reynolds number, hoping to locate Re_2 within a relative small range. It turned out that the solution always converged to an asymptotic periodic state for Re up to 15,000. Some of the characteristics of these periodic solutions for different Re are reported in Table IV. In Fig. 7, we illustrate the dependency of the periodic solutions, obtained by using 65×65 modes, on the Reynolds number. We find that the period of the asymptotic solutions increases almost linearly with respect to Re , while on the other hand, the

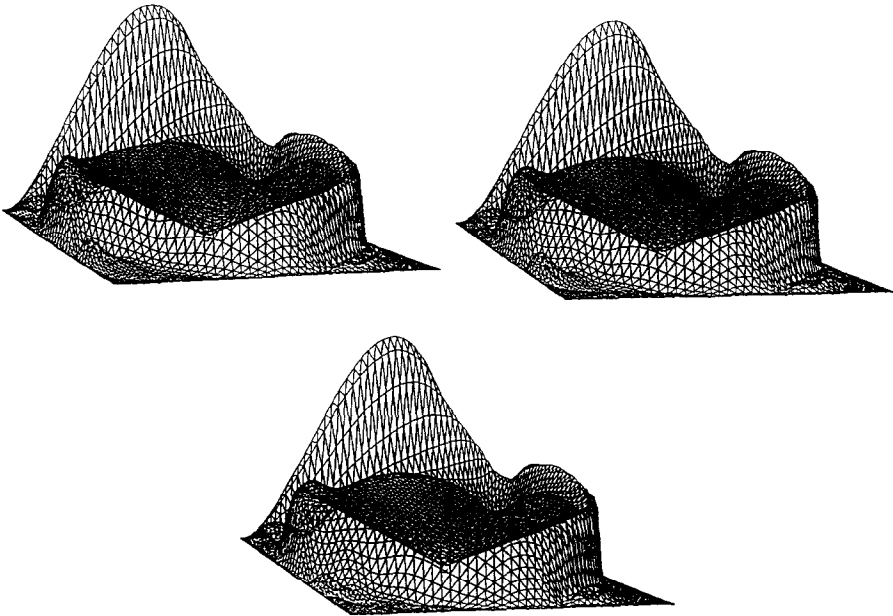


FIGURE 9—Continued

maximum and minimum kinetic energy decrease almost linearly with respect to Re (see Fig. 7).

As an example, we will present the results at $Re = 14,000$ in some detail. In Fig. 6, we present the phase diagrams and the spectral density of the kinetic energy and the first component of velocity at a particular point $(x, y) = (0.084, 0.990)$, based on the data taken at 50,000 time steps which are about 79 complete cycles. A complete cycle of a series of nine streamline contours at time interval of 1.59 is presented in Fig. 8. This time, the oscillation is much more pronounced throughout the domain: each of the secondary vortices at the top left and at the bottom left split up into two vortices and the two vortices rejoin each other to form a single vortex periodically in time; there are also significant oscillations inside the secondary and the tertiary vortices at the bottom right; a close look at the primary vortex shows that even the primary vortex is undergoing significant oscillations during each period. As a complement for the streamline contours, we plot a series of nine kinetic energy surfaces in Fig. 9 (data taken at the same time t as the corresponding streamline contour presented in Fig. 8) which give us a nice visualization of the momentum scale over the entire domain. From these surface plots one can observe a remarkable energy movement at the bottom left and at the bottom right. The oscillation of the kinetic energy distribution at the top left is also significant. Once again, the streamline contours and the surface of the kinetic energy at the beginning of the cycle are perfectly recaptured at the end of the cycle. Those plots indicate a perfect periodic state has been reached in this case.

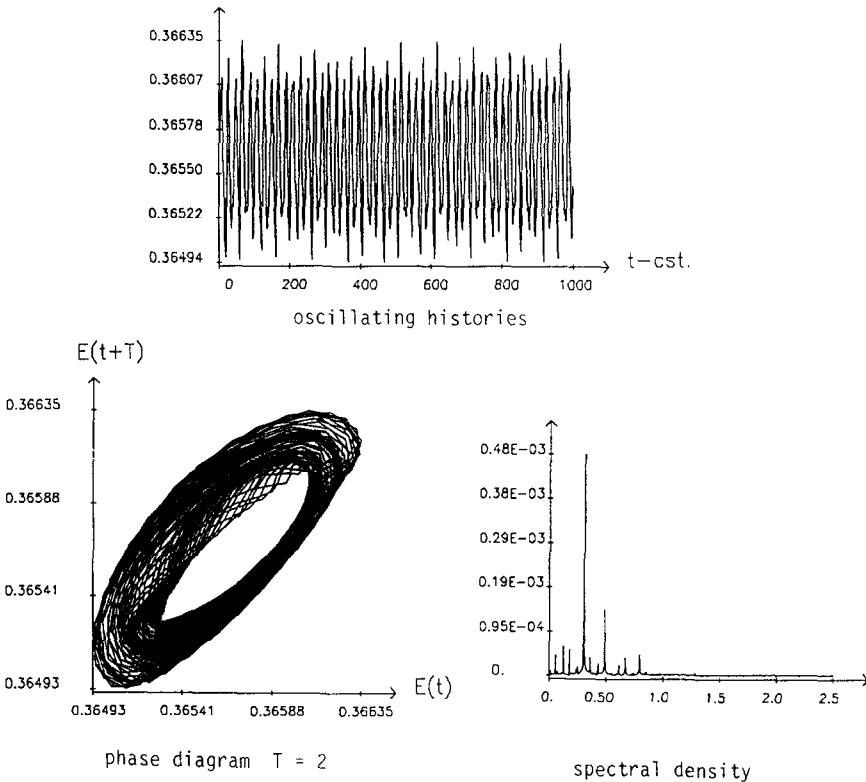


FIG. 10. Kinetic energy at $Re = 16,000$ with 65×65 modes.

We continued to increase the Reynolds number, taking the final asymptotic solution at $Re = 15,000$ as the initial data for $Re = 15,500$; we have run the scheme to as far as $t = 20,000$ and there was still no sign that the solution would converge to a periodic asymptotic state. The oscillating histories, the phase diagram, and the spectral density of the kinetic energy at $Re = 15,500$, based on the data from $t = 19,000$ to $t = 20,000$ are presented in Fig. 10. The phase diagram looks like a two-dimensional torus embedded in a higher dimensional space. The plot of the spectral density suggests that there are essentially two incommensurate active frequencies, which indicates that the flow is quasi-periodic, or more precisely, two-periodic.

4. CONCLUSION

By integrating the unsteady NSE, we have found that a Hopf bifurcation occurs at a critical Reynolds number in $(10,000, 10,500]$ for the regularized driven cavity flow. It seems that the periodic solutions we obtained for $Re \in [10,500, 15,000]$ are

not merely numerical artifacts because the computations made on a refined grid have given virtually the same results. At $Re = 15,500$, the computed solution loses time periodicity and becomes quasi-period, which indicates another bifurcation occurs at a critical Reynolds number in $(15,000, 15,500]$. It is almost certain that further increase of the Reynolds number would lead to a totally turbulent flow.

ACKNOWLEDGMENTS

This work was supported in part by NSF Grant DMS-8802596 and AFOSR-88013.

REFERENCES

1. C. H. BRUNEAU AND C. JOURON, *C. R. Acad. Sci. Paris*, **307**, 359 (1988).
2. C. CANUTO, M. Y. HUSSAINI, A. QUARTERONI, AND T. A. ZANG, *Spectral Methods in Fluid Dynamics* (Springer-Verlag, New York/Berlin, 1987).
3. A. FORTIN, M. FORTIN, AND J. J. GERVAIS, *J. Comput. Phys.* **70**, 295 (1987).
4. U. GHIA, K. N. GHIA, AND C. T. SHIN, *J. Comput. Phys.* **48**, 387 (1982).
5. J. W. GOODRICH, K. GUSTAFSON, AND K. HALASI, Hopf bifurcation in the driven cavity, *J. Comput. Phys.*, to appear.
6. K. GUSTAFSON AND K. HALASI, *J. Comput. Phys.* **70**, 271 (1987).
7. D. B. HAIDVOGEL AND T. A. ZANG, *J. Comput. Phys.* **30**, 167 (1979).
8. J. KIM AND MOIN, *J. Comput. Phys.* **59**, 308 (1985).
9. LE QUÉRÉ AND T. ALIZIARY DE ROQUEFORT, *J. Comput. Phys.* **57**, 210 (1985).
10. S. A. ORSZAG, *J. Comput. Phys.* **37**, 70 (1980).
11. J. SHEN, Thèse de Doctorat, Université de Paris-sud, 1987 (unpublished).
12. J. SHEN, *Model. Math. Anal. Num.* **22**, 677 (1988).
13. J. SHEN, *Comput. Methods Appl. Mech. Eng.* **80**, 273 (1990).
14. J. SHEN, "Projection Methods for Time Dependent Navier–Stokes Equations," *Appl. Math. Let.*, to appear.
15. R. TEMAM, *Navier–Stokes Equations. Theory and Numerical Analysis* (North-Holland, Amsterdam, 1979).
16. R. TEMAM, *Infinite Dimensional Dynamical Systems in Mechanics and Physics* (Springer-Verlag, New York, 1988).